Chemical Engineering Journal 430 (2022) 132769

Contents lists available at ScienceDirect

Chemical Engineering Journal

journal homepage: www.elsevier.com/locate/cej

Hybrid electrocatalyst Ag/Co/C via flash Joule heating for oxygen reduction reaction in alkaline media

Yishu Qiu [a,b,1], Zheng Hu [a,1], Hui Li [a,b], Qianqian Ren [a], Yanan Chen [c], Shi Hu [a,b,*]

[a] Tianjin Key Laboratory of Molecular Optoelectronic Science, Department of Chemistry, School of Science, Tianjin University, Tianjin 300072, PR China
[b] Institute of Energy, Hefei Comprehensive National Science Center, Hefei, Anhui 230026, PR China
[c] School of Materials Science and Engineering Key Laboratory of Advanced Ceramics and Machining Technology of Ministry of Education, Tianjin Key Laboratory of Composite and Functional Materials, Tianjin University, Tianjin 300072, PR China

ARTICLE INFO

Keywords:
Flash Joule heating
Silver
Oxygen reduction reaction

ABSTRACT

The commercial catalysts for oxygen reduction reaction (ORR) are highly dependent on the scarce and expensive Pt to achieve high activity and reasonable durability, especially for the fuel cells used in automobiles. Ag alloys have been proposed as promising candidates for non-Pt ORR catalysts in alkaline media, with reasonably high activity at significantly lower cost. Herein we demonstrate the synthesis of Ag/Co/C hybrid electrocatalyst for ORR via radiative flash Joule heating. Unlike the previously reported solid-solution structure of the quenched immiscible alloys by flash Joule heating, the large immiscibility gap in the liquid state of the Ag-Co alloy prevents the formation of solid solution. The hybrid catalyst exhibits a specific activity 40 times and a mass activity 52 times higher than that of the pristine Ag/C at 0.8 V vs. RHE in alkaline media, and its tolerance to methanol and ethanol is superior to that of commercial Pt/C. The enhanced activity and good stability are attributed to the enhanced oxygen adsorption energy on silver due to the strong interaction between silver and cobalt.

1. Introduction

During the past few decades, increasingly severe energy and environmental crisis have forced mankind to seek renewable resources and develop advanced technologies for clean energy, such as hydrogen production and conversion [1–3]. Proton exchange membrane fuel cell (PEMFC), a device that directly converts the stored chemical energy in hydrogen into electricity, is characterized by high energy density and low working temperature. It can be used in aerospace, automobiles, airplanes and other fields, and is regarded as the core of the "hydrogen economy" [4–10]. However, its large-scale commercialization is hindered by the cathodic oxygen reduction reaction (ORR), which is more than 6 orders of magnitude slower than the anodic hydrogen oxidation reaction [7,11,12]. Although the current state-of-the-art Pt-group metal (PGM) can achieve excellent ORR activity, the high cost caused by scarcity will account for 45% at 500,000 systems/year of total stack cost and is difficult to achieve 5,000-hour durability target, as predicted and tested by the Fuel Cell Technology Office of the Department of Energy (DOE) of United States [5,7,13–17]. Due to the severe dissolution and agglomeration problems in the acidic environment of PEMFC, it is very difficult to find other low-cost and high-activity catalysts to replace Pt, especially for the high Pt-loading fuel cells used in the automobiles [18]. In contrast, the anion exchange membrane fuel cell (AEMFC) based on alkaline systems provides a higher pH regime, making it possible to use the low-cost and earth-abundant elements in catalysts [19–22].

Silver (Ag), one of the less expensive and more abundant coin metals, stands out due to its acceptable ORR catalytic activity and superior electrochemical stability in alkaline environments [23–26]. However, its weak oxygen adsorption energy makes it less active than Pt [27]. A lot of efforts have been made to optimize the Ag-based catalysts, including alloying, hybrid fabrication, etc. It has been demonstrated that combining Ag with other transition metals with strong oxygen binding ability could enhance the activity through the fine-tuning of the d-band center [21,23,28–35]. As the cost of Ag is only about 2% of that of Pt ($27.12 to $1275.00 per troy oz, as of February 2021 respectively [36].), a reasonable improvement over the current technical merits could make Ag-based catalyst approach the target of replacing Pt in terms of cost performance.

* Corresponding author at: Tianjin Key Laboratory of Molecular Optoelectronic Science, Department of Chemistry, School of Science, Tianjin University, Tianjin 300072, PR China (S. Hu).
E-mail address: rychushi@gmail.com (S. Hu).
[1] These authors contributed equally to this work.

https://doi.org/10.1016/j.cej.2021.132769
Received 20 April 2021; Received in revised form 17 September 2021; Accepted 29 September 2021
Available online 6 October 2021

In this study, we fabricate a hybrid electrocatalyst of Ag/Co/C via radiative flash Joule heating, which possesses good activity and stability for ORR in alkaline media. Unlike the previously reported solid solution of Au-Ni and Ag-Cu [37,38], the high immiscibility gap in the Ag-Co phase diagram prevents the formation of quenched solid solution via flash Joule heating. The ultrafast cooling rate avoids the agglomeration of metallic nanoparticles during annealing, resulting in strong electronic interaction at the Ag-Co interface and improved oxygen adsorption energy on Ag. The activity of Ag/Co/C is superior to that of pristine Ag/C, Co/C, and thermally annealed Ag/Co/C, and approaches that of Pt/C at a much lower cost. Our work broadens the research scope of Joule heating from single-atom catalysts [39], metallic nanoparticles (NPs) [40], bimetallic alloys [41], and high-entropy alloys [37] to hybrid catalysts with strong metal-substrate interaction (SMSI) [42,43], which may help to further improve the performance of the earth-abundant ORR catalysts.

2. Experimental sections

2.1. Chemicals

All chemicals were used as received. Silver nitrate ($AgNO_3$, AR, 99.8%), Silver acetate ($AgC_2H_3O_2$, AR, 99.5%), and potassium hexacyanocobaltate(III) ($K_3[Co(CN)_6]$, 98%) were purchased from Aladdin. Vulcan XC-72R carbon was supplied by Cabot Corp. Potassium hydroxide (KOH, 95%) was obtained from Meryer. 5 wt% nafion solution in lower alcohols was purchased from Sigma-Aldrich. Commercial Pt/C (20 wt%) was supplied by Hesen Electric Co., Ltd. Ethanol was obtained from Sinopharm Chemical Reagent Co., Ltd. Ultrapure water was used throughout the experiment.

2.2. Catalyst synthesis

The carbon-supported $Ag_3[Co(CN)_6]$ nanoparticles (NPs) precursor was synthesized from $AgNO_3$ and $K_3[Co(CN)_6]$ by multistage incipient-wetness impregnation, as reported previously [23]. Briefly, 2 ml of $K_3[Co(CN)_6]$ (0.0831 g) aqueous solution and 2 ml of $AgNO_3$ (0.1911 g) were added to 0.11 g of Vulcan XC-72R carbon alternately (1 ml each time and dried at 60 °C), for four impregnation/drying cycles in total. Then the powder was washed three times with deionized water to remove excess $AgNO_3$ and KCN. Finally, the $Ag_3[Co(CN)_6]$ precursor was obtained after freeze-drying overnight. In a typical process of the Joule heating, about 0.01 g of precursor powder was sandwiched between two pieces of carbon paper (1 cm by 2 cm), connected to copper tapes with conductive silver paste and suspended on a glass plate. The samples were sealed in a chamber filled with Ar and the copper tapes connected to a direct-current power source to allow a current of 20 A to flow for 0.5 s.

The catalysts Ag/C and Co/C were prepared by adding 0.055 g of Vulcan XC-72R to 4 ml of 0.11 M $AgC_2H_3O_2$ aqueous solution (heated to 60 °C to promote dissolution) and 4 ml of 0.20 M $K_3[Co(CN)_6]$ aqueous solution respectively, ultrasonicated for 1 h and freeze-dried overnight, before the same Joule heating procedures were taken.

For comparison, annealed Ag/Co/C was prepared by holding 20 mg of carbon-supported $Ag_3[Co(CN)_6]$ NPs precursor at 500 °C (the heating rate was 5 °C/min) under 4% H_2/Ar for ten minutes and cooled to room temperature within the furnace.

2.3. Characterizations

The morphology was characterized by transmission electron microscopy (TEM, JEOL-1230) and high-resolution TEM (HRTEM, JEOL JEM-F200) equipped with energy dispersive spectroscopy (EDS). The crystal structure was investigated by X-ray diffraction (XRD) on a D8-Focus diffractometer (Bruker AXS) employing Cu Kα radiation (λ = 1.5418 Å). The surface composition and chemical state were acquired by X-ray photoelectron spectroscopy (XPS) using a Thermo Fisher Scientific Escalab 250 Xi spectrometer with Al Kα excitation. The graphitization degree of carbon was detected by HORIBA Scientific LabRAM HR Evolution. The element content was obtained from inductively coupled plasma optical emission spectrometry (ICP-OES, Agilent 720).

2.4. Electrochemical measurements

The electrochemical studies were performed on an electrochemical workstation (CS-150H workstation from Wuhan Corrtest Instrument Co. Ltd. China) equipped with a rotating disk electrode. To prepare the working electrode, 2 mg of catalyst was dispersed in 990 μl of mixed solvent (690 μl of ethanol and 300 μl of pure water) with additional 10 μl of 5 wt% Nafion solution by ultrasonic for at least 1 h to form a homogeneous ink. Then 6 μl of the ink was dripped onto a cleaned 4 mm (0.1256 cm^2) glassy carbon rotating disk electrode and the solvent was evaporated at room temperature. A Pt plate and Hg/HgO electrode (in 1 M KOH) were used as the counter electrode and reference electrode, respectively. All the tests were conducted at room temperature in 1 M KOH. All the potentials obtained were in reference to the reversible hydrogen electrode (RHE) by adding a value of (0.059 × pH + 0.098) V.

Cyclic voltammogram (CV) from 0 to 1.0 V vs. RHE at 200 mV/s was performed in Ar-saturated 1 M KOH to clean and activate the electrode firstly. The oxidation/reduction for Ag was identified by cycling from 0 to 1.4 V vs. RHE at 20 mV/s for three cycles. Then the ORR measurements were performed in O_2-saturated 1 M KOH at 10 mV/s with different rotation speeds from 400 rpm to 2500 rpm. The electrochemical impedance (EIS) test was performed at 0.825 V vs. RHE in O_2-saturated 1 M KOH at 1600 rpm with frequency ranging from 1 to 10^5 Hz.

Turnover frequency (TOF) was calculated by the following equation [3,44]:

$$TOF = \frac{I}{4NF} \quad (d)$$

where I is the measured current (A), F is the Faraday constant (96485 C mol^{-1}), and N is the number of active sites (mol). The factor 1/4 represents the four electrons required to form four hydroxyl ions from one oxygen molecule ($O_2 + 2H_2O + 4e^- \rightarrow 4OH^-$).

The electron transfer number (n) was calculated according to the Koutecky-Levich (K-L) equation [45] at different potentials:

$$j^{-1} = j_L^{-1} + j_K^{-1} \quad (a)$$

$$j_L = 0.2nFC_0D_0^{2/3}\nu^{-1/6}\omega^{1/2} \quad (b)$$

$$j_K = nFkC_0 \quad (c)$$

where j is the measured current density (mA cm^{-2}), j_L and j_K are the diffusion limiting and kinetic current densities, ω is the electrode rotation speed (rpm), n is the electron transfer number, F is the Faraday constant (96485 C mol^{-1}), C_0 is the bulk concentration of O_2 in 1 M KOH (8.429×10^{-4} mol L^{-1}), D_0 is the diffusion coefficient of O_2 in 1 M KOH (1.43×10^{-5} cm^2 s^{-1}), ν is the kinematic viscosity of 1 M KOH (0.01074 cm^2 s^{-1}) [46], and k is the electron transfer rate constant (mol cm^3 s^{-1}).

Long-term stability was tested by cycling from 0.6 to 1.0 V vs. RHE at 50 mV/s for 2000 cycles in O_2-saturated 1 M KOH. The ORR polarization curve was taken after 2000 cycles in a fresh batch and compared with the initial curve.

2.5. Density functional theory (DFT) calculation

The ORR reaction pathway was performed by the Vienna ab initio simulation package (VASP) [47]. Perdew–Burke–Ernzerhof (PBE)-Generalized gradient approximation (GGA) functional was used to describe the exchange–correlation part in the KS-DFT equation. The

plane-wave basis sets with an energy cutoff of 400 eV were selected. And the criteria of self-consistent calculation and ionic step were chosen as 1×10^{-8} eV and 0.01 eV Å^{-1}. The Ag (1 1 1) facet and Co (1 1 1) facet were used to modeling the slab model with vacuum width of 15 Å between the slabs along the Z-axis. The Brillouin zone was sampled by 6 × 6 × 1 Monkhorst–Pack mesh k-points for surface calculation and charge analysis. The oxygen adsorption free energy ΔG_{O^*} was calculated by

$$\Delta G_{O^*} = E(surf + O) - E(surf) - (E(H_2O) - E(H_2)) + \Delta E_{ZPE} - T\Delta S$$

where ΔE_{ZPE} and ΔS are the difference in the zero-point energy and entropy between the adsorbed O atom and the gaseous phase O_2. The thermodynamic modification of the energy of gas molecules and adsorbed states was completed by vaspkit [48]. The free energy of $H^+(10^{-14}$ M) + e^- can be obtained by adding a correction energy in pH [49]: $\Delta G(\mathrm{pH}) = kTln[H^+] = -\mathrm{pH}{\cdot}kTln10$, where pH = 14.

3. Results and discussion

3.1. Structural characterization of Ag/Co/C electrocatalyst

While the previous Joule-heating synthesis of binary immiscible alloy systems of Au-Ni, Cu-Ag, etc. always quench the solid solution structure, the high immiscibility of Ag-Co system only leads to the formation of heterostructure, as predicted by the phase diagram (Fig. 1a). The immiscibility gap is huge even at the liquid state. During the flash Joule heating, the $Ag_3[Co(CN)_6]$/C NPs precursor was subjected to a 0.5-s high-temperature pulse, during which the glaring carbon papers are shown in Fig. 1b. The dazzling light on the carbon paper indicates its high temperature during the Joule heating process, and the intense heat radiation causes the precursor to decompose immediately. The cooling process is shown by the blue arrow in Fig. 1a. The rapid quenching avoids the agglomeration of the nanoparticles during cooling, assisted by the surface defects on the carbon black (CB). From the representative TEM image of the Ag/Co/C hybrid structure (Fig. 1c), particles with an average size of 28 ± 15 nm are uniformly dispersed on the surface of CB. The average sizes of the annealed Ag/Co/C and Ag/C are 37 nm and 12 nm respectively, as shown in Figure S1a–b. The pristine Co NPs are less discernable in the TEM image of Co/C (Figure S1c). Due to Ostwald ripening, Ag/Co NPs are larger than pristine Ag and Co. However, rapid quenching during the Joule heating effectively prevents further growth during annealing. The HRTEM image in Fig. 1d shows a tightly integrated interface with two characteristic spacings of 0.24 nm and 0.20 nm, which match well with Ag (1 1 1) and Co (1 1 1), respectively. Fig. 1e–g are EDS maps of Ag/Co/C NPs. The overlay of Ag and Co maps indicates a clear separation of the two elements and further confirms the hybrid structure.

The XRD patterns of the $Ag_3[Co(CN)_6]$/C precursor (Fig. 2a) shows no impurity peaks in the 2θ range of 30°−80°, confirming the high purity of the precursor. As for Ag/Co/C sample, peaks at 38.1°, 44.2°, 64.4° and 77.4° can be indexed to the (1 1 1), (2 0 0), (2 2 0) and (3 1 1) planes of face-centered cubic Ag (JCPDS#04–0783). The minimal shift of the diffraction peaks to low angle indicates that the sample have undergone minimal alloying during the ultrafast cooling process [51]. The two peaks at 44.2° and 51.4° are assigned to the (1 1 1) and (2 0 0) planes of Co (JCPDS#15–0806). The weak signal of Co can be attributed to its low content according to the result of ICP-OES (Table S1) and relatively small size, which is also suppressed by the strong Ag signal. According to the EDS mapping of Co, there are some very small Co clusters dispersed on the carbon black. The XRD peak positions of the annealed Ag/Co/C, Ag/C, and Co/C agree with those of Ag (JCPDS#04–0783) and Co (JCPDS#15–0806), as shown in Figure S2a – c, confirming the successful preparation of the hybrid catalysts on carbon.

The XPS spectra survey in Fig. 2b indicates the existence of C, N, O, Ag and Co elements. The two peaks at 368.7 eV and 374.7 eV are observed in the high-resolution spectrum of Ag 3d (Fig. 2c), corresponding to Ag $3d_{5/2}$ and $3d_{3/2}$ with a spin–orbit splitting of 6.0 eV, which matches metallic Ag (Ag^0). As compared with Ag/C (Figure S3), the corresponding peaks shift towards the higher binding energy by 0.3 eV, indicating electron accumulation on Ag through the interaction with Co at the Ag/Co interface. In the high-resolution spectrum of Co 2p

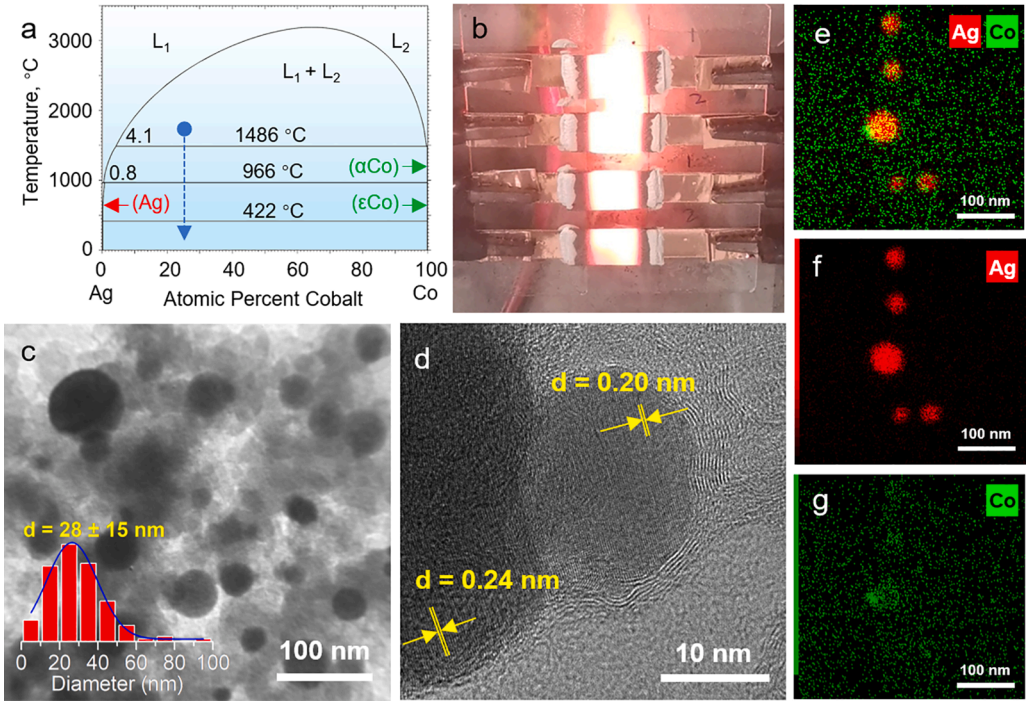

Fig. 1. (a) Ag-Co phase diagram, adapted from reference [50]. The arrow indicates the cooling process during the synthesis. (b) The photo of radiative Joule-heating process for the synthesis of Ag/Co/C. (c) Low-magnification TEM image of Ag/Co/C (inset: histograms for particle size distribution of Ag/Co/C). (d) HRTEM image of Ag/Co/C. (e–g) EDS maps of Ag/Co/C.

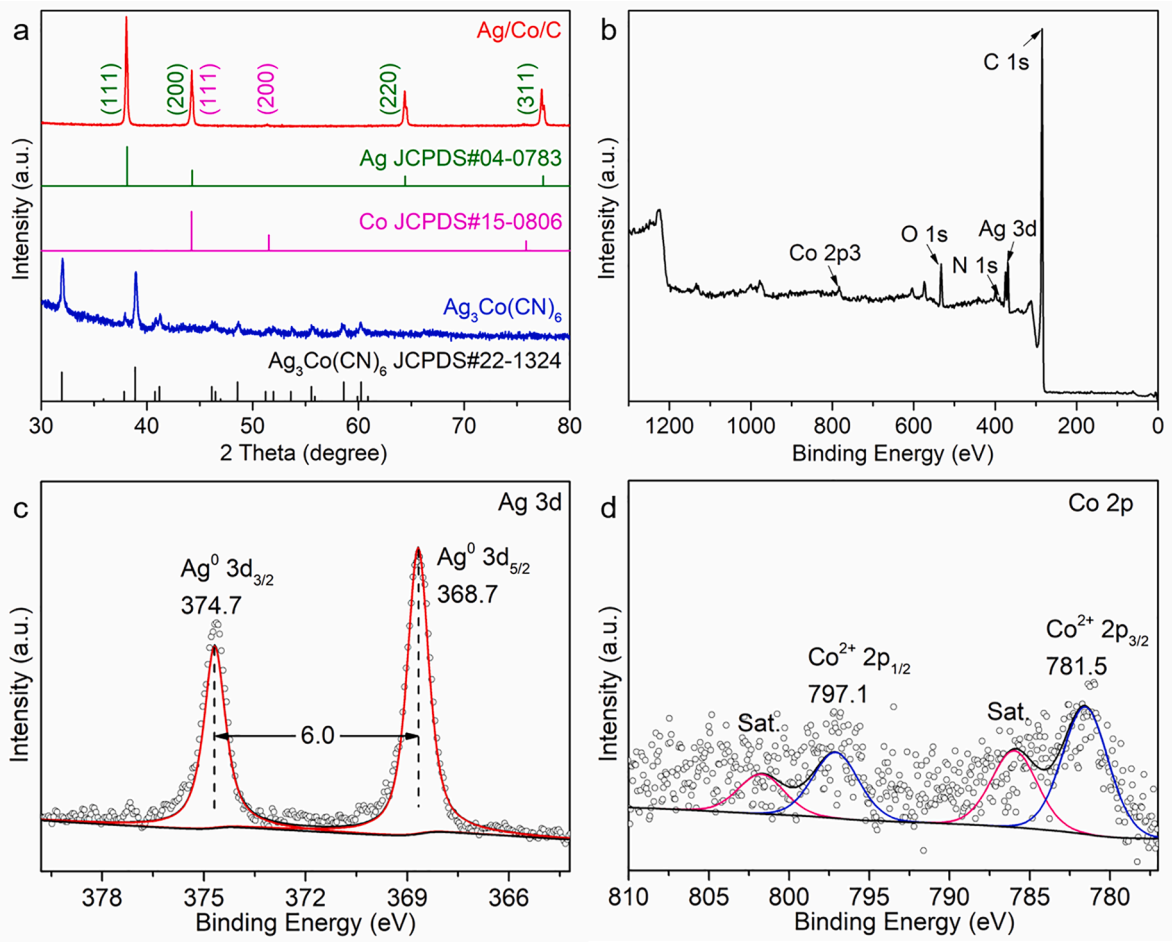

Fig. 2. (a) XRD patterns of $Ag_3[Co(CN)_6]$ and Ag/Co/C. (b) Survey XPS spectrum, (c) high resolution Ag 3d XPS spectrum, and (d) high resolution Co 2p XPS spectrum of Ag/Co/C.

(Fig. 2d), the Co $2p_{3/2}$ (781.5 eV) and Co $2p_{1/2}$ (797.1 eV) with their shake-up satellite peaks correspond to Co^{2+}, attributing to the surface-oxidized Co due to exposure to the ambient atmosphere. The photoelectron signal for Co at the Ag/Co interface can hardly be collected and is easily covered by abundant Co^{2+} signal on the surface. Therefore, the Co^{2+} signal dominates the Co XPS. In the Raman spectra, the D-band arises from disorder of carbon, while the G-band represents the ordered part [52]. The degree of graphitization is inversely proportional to the D/G ratio (I_D/I_G). The I_D/I_G of Ag/Co/C, annealed Ag/Co/C and Vulcan XC-72R carbon are all close to 1 as shown in Figure S4, indicating the similar low graphitization degree, which excludes the possible impact of changes in the carbon substrate on the performance of the catalysts.

3.2. Catalytic activity of Ag/Co/C in ORR

The CV curves in Fig. 3a reveal the surface composition of the electrocatalysts. Three characteristic oxidation peaks of Ag/C at 1.15, 1.23, and 1.30 V vs. RHE represent the formation of Ag_2O monolayer, AgOH bulk, and Ag_2O bulk [29]. The Ag oxides are reduced at 1.12 V (vs. RHE) for Ag/C and 1.09 V for Ag/Co/C in the negative scan, respectively, indicating an enhanced interaction between the adsorbed oxygenated species on Ag/Co/C [28]. As the oxygen adsorption energy on the pristine Ag is on the weaker side of volcano plot [27], the result indicates that carbon-supported Ag could become more active for ORR at the presence of cobalt.

The ORR activities of Ag/Co/C, annealed Ag/Co/C, Ag/C, Co/C, and Pt/C catalysts are first characterized by linear scanning voltammetry (LSV) curves in O_2-saturated 1 M KOH (Fig. 3b). Detailed data are listed in Table 1. Compared with Ag/C and Co/C electrocatalysts, the activity of Ag/Co/C is higher, with more positive onset potential (E_{onset} = 0.92 V vs. RHE), larger half-wave potential ($E_{1/2}$ = 0.85 V vs. RHE), and larger limiting current density ($|j_L|$ = 3.48 mA cm^{-2}, within the 10% margin of the theoretical j_L), indicating that the synergistic effect of Ag and Co is crucial to the improvement of ORR activity. The Ag/Co/C synthesized by Joule heating also exhibits superior activity than Ag/Co/C prepared by traditional annealing process, which is inseparable from the reduction of agglomeration during the preparation. Moreover, the Tafel slope (Fig. 3c) of Ag/Co/C is 38.49 mV dec^{-1}, significantly smaller than that of Pt/C (64.17 mV dec^{-1}) and Ag/C (90.79 mV dec^{-1}), confirming the enhancement effect of Ag/Co/C in ORR dynamics. Besides, Ag/Co/C exhibits the smallest semicircular diameter compared with that of Ag/C and commercial Pt/C in the electrochemical impedance spectroscopy (EIS, Fig. 3d), which could originate from the SMSI that facilitates the charge transfer and improves the conductivity of Ag/Co/C during ORR process.

Fig. 3e shows the TOF plots, which are positively correlated with the intrinsic activity of the active sites (the detailed calculation process can refer to discussion S1). The TOF of Ag/Co/C is 0.03 s^{-1} at 0.8 V, which is lower than that of Pt/C (0.10 s^{-1} at 0.8 V), but 3 times larger than that of annealed Ag/Co/C and Ag/C (0.01 s^{-1} at 0.8 V), indicating the increased intrinsic activity of Ag/Co/C due to the synergistic effect of Ag and Co.

The electrochemical active surface area (ECSA) of Pt/C is evaluated by integrating the charge in the hydrogen underpotential deposition region (Figure S5a), based on the theoretical charge of 210 μC cm^{-2} for a hydrogen monolayer adsorption [53]. The ECSAs of Ag/C, Ag/Co/C, and annealed Ag/Co/C (Figure S5b) are estimated by integrating the Ag

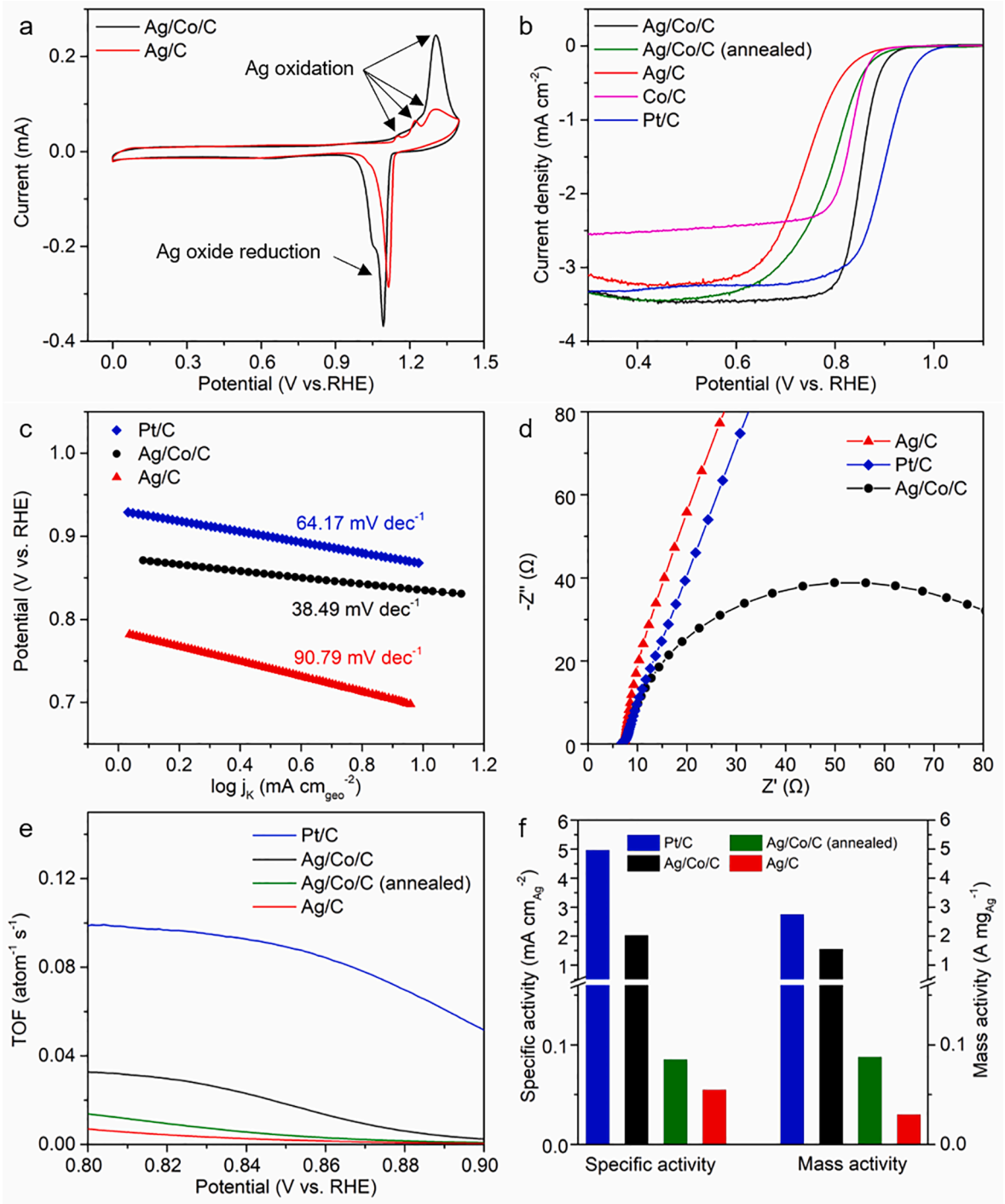

Fig. 3. (a) CV curves of Ag/C and Ag/Co/C in Ar-saturated 1 M KOH at a scan rate of 20 mV s^{-1}. (b) The ORR polarization curves of Ag/Co/C, annealed Ag/Co/C, Ag/C, Co/C, and commercial Pt/C at 10 mV/s with a rotation speed of 1600 rpm. (c) Tafel plots of Ag/Co/C, Ag/C, and commercial Pt/C. (d) EIS plots toward ORR with a test voltage of 0.825 V vs. RHE at 1600 rpm. (e) TOF plots of Ag/Co/C, annealed Ag/Co/C, Ag/C, and commercial Pt/C. (f) Specific activities and mass activities at 0.8 V vs. RHE of Ag/Co/C, annealed Ag/Co/C, Ag/C, and commercial Pt/C.

oxide reduction charge and using theoretical value of 400 μC cm^{-2} [25]. The specific activities (SAs) are calculated by normalizing the kinetic current at 0.8 V vs. RHE to ECSA. And the mass activities (MAs) are estimated via the normalization of the kinetic current at 0.8 V to Ag-loading on the electrode (Pt-loading for Pt/C). As shown in Fig. 3f, the SAs decrease in the following order: Pt/C (4.96 mA cm_{Pt}^{-2}) > Ag/Co/C (2.03 mA cm_{Ag}^{-2}) > annealed Ag/Co/C (0.09 mA cm_{Ag}^{-2}) > Ag/C (0.05 mA cm_{Ag}^{-2}). The MAs also show the same trend. Ag/Co/C exhibits a MA of 1.55 A mg_{Ag}^{-1}, more than half that of Pt/C (2.75 A mg_{Pt}^{-1}), and 17 times that of annealed Ag/Co/C (0.09 A mg_{Ag}^{-1}) and 52 times that of Ag/C (0.03 A mg_{Ag}^{-1}). Considering the cost of Ag is only about 2% of that of Pt, the greatly improved activity of Ag/Co/C makes it expected to be a substitute for Pt catalyst in ORR.

The ORR in aqueous solution can proceed via a 2-electron pathway or a 4-electron pathway. In the 4-electron pathway, oxygen species can be converted directly into OH^- in alkaline media, which is the preferred pathway on the fuel cell cathode [45]. The electron transfer number (n) can be calculated from the K-L equations. The LSV curves of Ag/Co/C

Table 1
Summary of ORR activities of Ag/Co/C, annealed Ag/Co/C, Ag/C, Co/C, and Pt/C.

Sample	Catalyst loading (mg cm^{-2})	E_{onset} [a] (V)	$E_{1/2}$ (V)	$\|j_L\|$ [b] (mA cm^{-2})
Ag/Co/C	0.10	0.92	0.85	3.48
Ag/Co/C (annealed)	0.10	0.90	0.79	3.41
Ag/C	0.10	0.87	0.74	3.21
Co/C	0.10	0.88	0.83	2.48
Pt/C	0.08	0.99	0.90	3.25

[a] Onset potential was obtained at an ORR current density of 0.1 mA cm^{-2}.
[b] Limiting current density was acquired at 0.5 V vs. RHE. Theoretical j_L was calculated as 3.26 mA cm^{-2} in 1 M KOH at 1600 rpm for a four-electron transfer pathway according to Levich equation.

are collected with different rotation speeds from 400 rpm to 2500 rpm in O_2-saturated 1 M KOH (the inset of Fig. 4a). From the K-L plots (j^{-1} vs $\omega^{-1/2}$) obtained at different voltages (Fig. 4a), the value of n is determined as ~ 4.3, indicating that the ORR at Ag/Co/C occurs predominantly via a four-electron pathway. The long-term stability is assessed by repeating cycling from 0.6 to 1.0 V vs. RHE at 50 mV/s in O_2-saturated 1 M KOH. What's more, the half-wave potential of Ag/Co/C is only negatively shifted by ca. 10 mV after 2000 cycles in oxygen (Fig. 4b), on the contrary, it is negatively shifted by 38 mV for commercial Pt/C under the same conditions (Figure S6). The excellent stability of Ag/Co/C could be attributed to the SMSI brought by the Joule heating method. It is inferred from the TEM image of Ag/Co/C after the stability test (Figure S7) that the main reason for the decrease of ORR activity is presumed to be a small amount of catalyst degraded over time. One haunting problem for the alkaline direct alcohol fuel cell is the cathode poisoning by alcohols [24]. As shown in Fig. 4 d–f, the ORR polarization curve of Ag/Co/C is almost unaffected in the presence of 0.01 M methanol or ethanol, while that of the commercial Pt/C is severely poisoned by the alcohol under the same conditions (Figure S8a–b).

First principle calculation is applied to study the mechanism of surface reaction. Firstly, the reaction pathways happened on Ag and Co surface are calculated and plotted in Fig. 5a and 5b. In view of thermodynamics, the limiting potential of Ag in overall ORR reaction pathway is lower than that of Co, which indicates that Ag nanoparticle surface in the heterostructure should be the active sites. Especially, the O binding energy (ΔG(O*)) is studied and the Co sites have more negative ΔG(O*) than the Ag sites, which is attributed to the difference of oxygen affinity between Ag and Co. According to the previous study [54], the Ag surface is favorable for oxygen spillover, which enhances the ORR kinetics. The calculated O_2 dissociation barrier at the Ag sites is close to zero (-0.11 eV), validating this hypothesis. What's more, based on d-band center theory, the spillover could be further enhanced [55] because Ag is negatively charged according to the XPS data. The Ag/CoO_x model can also be constructed to study the *in-situ* structure in the ORR reaction (Figure S9). Based on the Fukui index analysis (Fig. 5c), the Co sites have the most negative f(+) and correspondingly highest

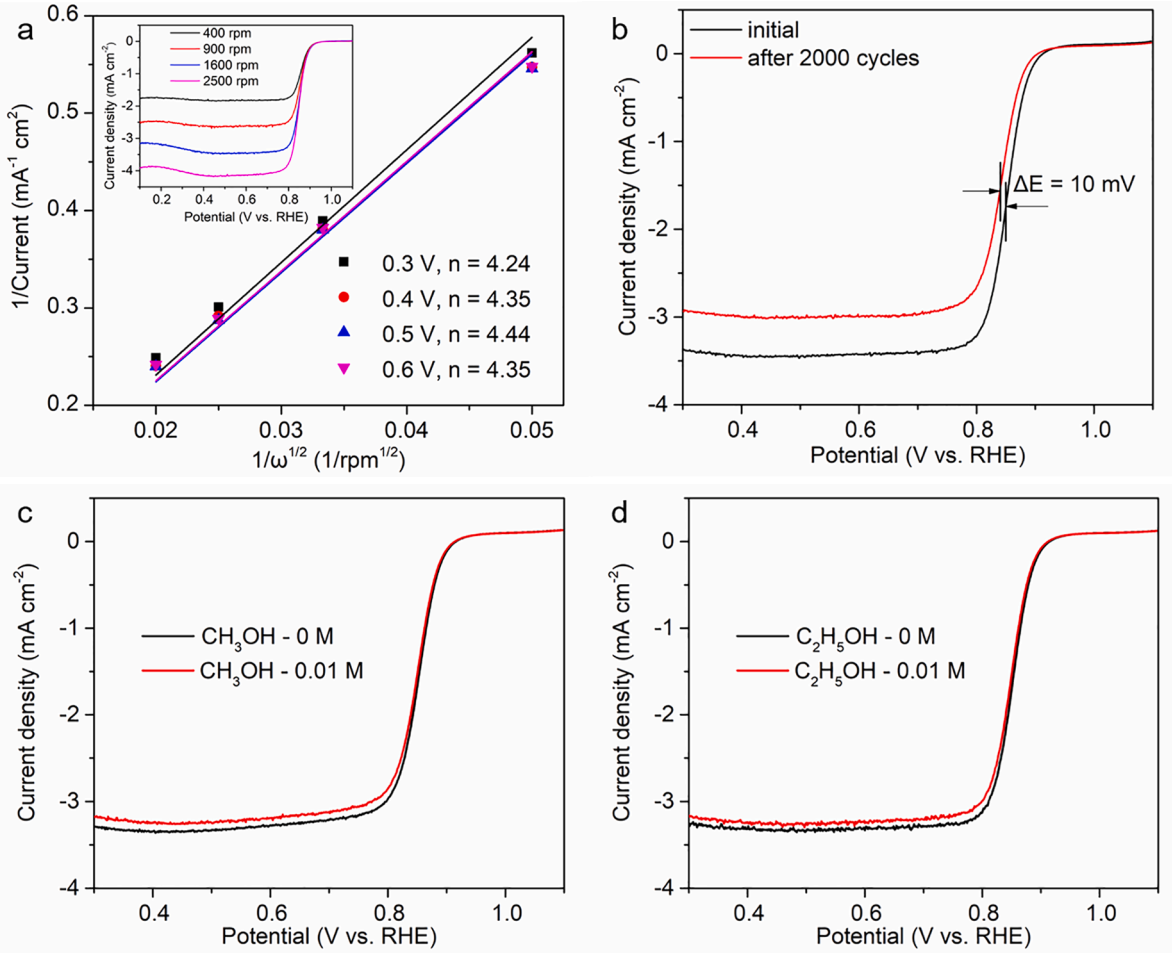

Fig. 4. (a) Koutecky-Levich plots showing electron transfer number for Ag/Co/C at different voltages. Inset: the ORR polarization curves of Ag/Co/C at 10 mV/s with rotation speeds of 400 rpm, 900 rpm, 1600 rpm, and 2500 rpm. (b) The ORR polarization curves of Ag/Co/C in O_2-saturated 1 M KOH at 10 mV/s with a rotation speed of 1600 rpm before (black line) and after (red line) 2000 cycles from 0.6 to 1.0 V vs. RHE. The ORR polarization curves of Ag/Co/C in O_2-saturated 1 M KOH at 10 mV/s with a rotation speed of 1600 rpm with or without containing 0.01 M (c) methanol and (d) ethanol.

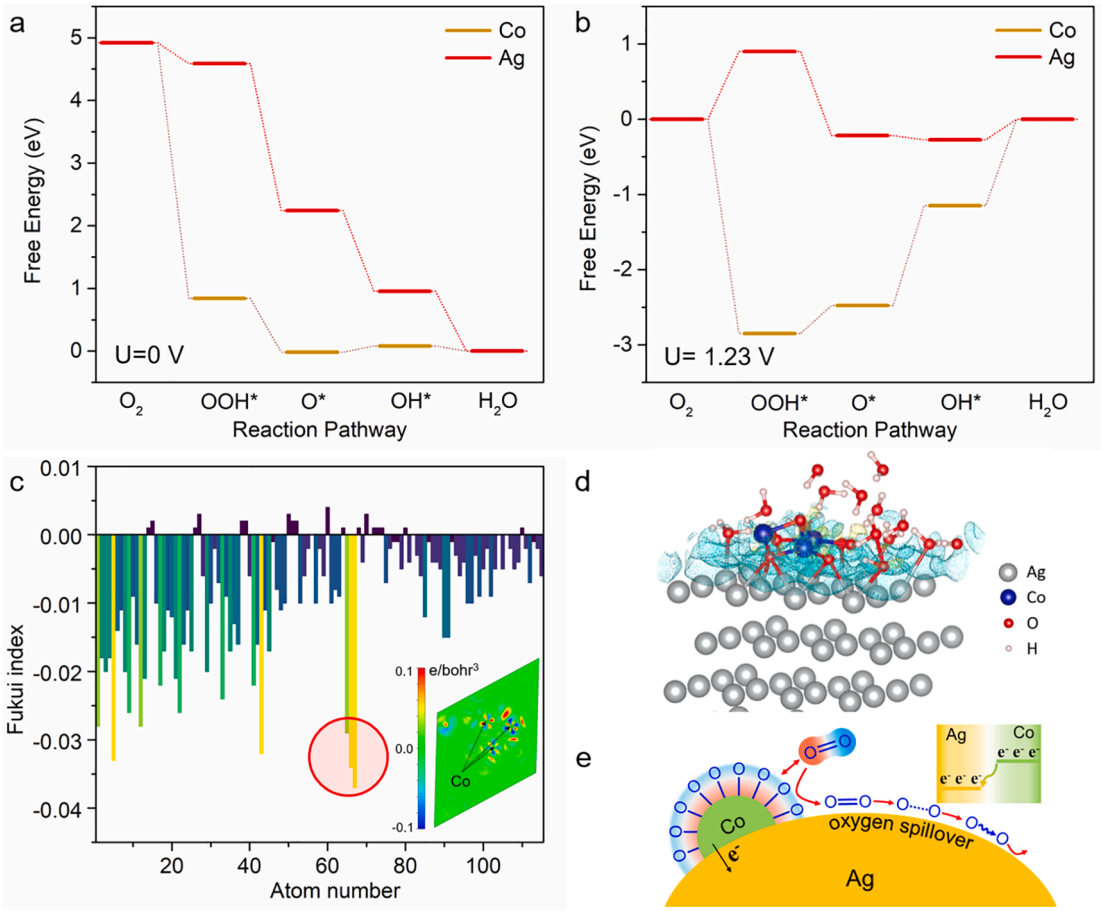

Fig. 5. (a-b) Simulated ORR reaction pathway when U = 0 V and U = 1.23 V. (c) Histogram of simulated Fukui index in all-atom with the inset of Fukui index distribution on the Co sites. (d) The simulated differential charge of the Ag/CoO_x model (blue: accepting electrons, yellow: donating electrons). (e) Schematic illustration of the proposed ORR mechanism on Ag/Co/C catalyst. Inset: the charge transfer occurs at the Ag/Co interface due to the difference of their work function.

activity for the nucleophilic attack of O_2. Differential charge analysis (Fig. 5d) and observed dynamic equilibrium between initial Co-O bond and new Co-O_2 bond in the AIMD simulation (Supplementary movie) also demonstrate the strong interaction between O_2 molecule and Co sites. In this sense, Co sites not only play a role in the polarization of the neighbor Ag sites, but also promote the interaction between the catalysts and O_2(g). Combined with the above analysis, the proposed ORR mechanism on Ag/Co/C catalyst is shown in Fig. 5e. The ORR reaction starts from the approaching of O_2 to the surface and polarization caused by the strong interaction between Co and O. Then Co-Ag interaction further enhances the O spillover on Ag surface and thus promotes the O_2 dissociation kinetics. The following ORR sub-steps on the Ag surface are featured with a small barrier. To sum up, the Joule heating method creates a good interface between Ag and Co and facilitates the Ag-Co synergy, which boosts the ORR kinetics on the Ag-sites.

4. Conclusion

In summary, an ultrafast synthetic strategy–radiative flash Joule heating has been developed to synthesize a hybrid catalyst of Ag/Co/C, which is featured by electron accumulation and strengthening of the oxygen adsorption energy on Ag. The catalyst shows an onset potential of 0.92 V vs. RHE, a half-wave potential of 0.85 V, a specific activity of 2.03 mA cm_{Ag}^{-2} and a mass activity of 1.55 A mg_{Ag}^{-1} at 0.80 V in 1 M KOH. Its highly-reduced cost (2% of Pt/C) and excellent tolerance to methanol and ethanol make it a promising alternative to Pt/C, especially in cost-sensitive situations. Different from the previous reports on quenched solid solution of immiscible alloy, this work demonstrates the synthesis of hetero-structured electrocatalysts with SMSI, which could be extended to the design of other catalysts.

Declaration of Competing Interest

The authors declare that they have no known competing financial interests or personal relationships that could have appeared to influence the work reported in this paper.

Acknowledgements

This work was financially supported by the Natural Science Foundation of Tianjin, China under No. 18JCYBJC20600 and Institute of Energy, Hefei Comprehensive National Science Center (No. 19KZS207).

Appendix A. Supplementary data

Supplementary data to this article can be found online at https://doi.org/10.1016/j.cej.2021.132769.

References

[1] Y. Hu, D. Huang, J. Zhang, Y. Huang, M.-S. Balogun, Y. Tong, Dual doping induced interfacial engineering of Fe_2N/Fe_3N hybrids with favorable d-band towards efficient overall water splitting, ChemCatChem 11 (24) (2019) 6051–6060.
[2] Y. Huang, L. Hu, R. Liu, Y. Hu, T. Xiong, W. Qiu, M.S. Balogun, A. Pan, Y. Tong, Nitrogen treatment generates tunable nanohybridization of Ni_5P_4 nanosheets with nickel hydr(oxy)oxides for efficient hydrogen production in alkaline, seawater and acidic media, Appl. Catal. B 251 (2019) 181–194.

[3] Y. Hu, T. Xiong, M.S.J.T. Balogun, Y. Huang, D. Adekoya, S. Zhang, Y. Tong, Enhanced metallicity boosts hydrogen evolution capability of dual-bimetallic Ni–Fe nitride nanoparticles, Materials Today Physics 15 (2020), 100267.

[4] M. Shao, Q. Chang, J.-P. Dodelet, R. Chenitz, Recent advances in electrocatalysts for oxygen reduction reaction, Chem Rev 116 (6) (2016) 3594–3657.

[5] D. Banham, S. Ye, Current status and future development of catalyst materials and catalyst layers for proton exchange membrane fuel cells: an industrial perspective, ACS Energy Lett. 2 (3) (2017) 629–638.

[6] Z. Liu, Z. Zhao, B. Peng, X. Duan, Y. Huang, Beyond extended surfaces: understanding the oxygen reduction reaction on nanocatalysts, J Am Chem Soc 142 (42) (2020) 17812–17827.

[7] M.K. Debe, Electrocatalyst approaches and challenges for automotive fuel cells, Nature 486 (7401) (2012) 43–51.

[8] S. Zaman, L. Huang, A.I. Douka, H. Yang, B. You, B.Y. Xia, Oxygen reduction electrocatalysts toward practical fuel cells: progress and perspectives, Angew Chem Int Ed Engl 60 (2021) 2–23.

[9] P. Su, W. Huang, J. Zhang, U. Guharoy, Q. Du, Q. Sun, Q. Jiang, Y.i. Cheng, J. Yang, X. Zhang, Y. Liu, S.P. Jiang, J. Liu, Fe atoms anchored on defective nitrogen doped hollow carbon spheres as efficient electrocatalysts for oxygen reduction reaction, Nano Res. 14 (4) (2021) 1069–1077.

[10] P.Y. You, S.K. Kamarudin, Recent progress of carbonaceous materials in fuel cell applications: an overview, Chem. Eng. J. 309 (2017) 489–502.

[11] R. Ding, Y. Liu, Z. Rui, J. Li, J. Liu, Z. Zou, Facile grafting strategy synthesis of single-atom electrocatalyst with enhanced ORR performance, Nano Res. 13 (6) (2020) 1519–1526.

[12] J. Ma, L. Wang, Y. Deng, W. Zhang, T. Wu, Y. Song, Mass production of high-performance single atomic FeNC electrocatalysts via sequenced ultrasonic atomization and pyrolysis process, Sci. China Mater. 64 (3) (2021) 631–641.

[13] B.F. Vojislav R. Stamenkovic, Bongjin Simon Mun, Guofeng Wang, Philip N. Ross, Christopher A. Lucas, Nenad M. Marković, Improved Oxygen Reduction Activity on Pt3Ni(111) via Increased Surface Site Availability, Science 315 (2007) 493-497.

[14] C. Wang, N.M. Markovic, V.R. Stamenkovic, Advanced platinum alloy electrocatalysts for the oxygen reduction reaction, ACS Catal. 2 (5) (2012) 891–898.

[15] L. Su, W. Jia, C.-M. Li, Y. Lei, Mechanisms for enhanced performance of platinum-based electrocatalysts in proton exchange membrane fuel cells, ChemSusChem 7 (2) (2014) 361–378.

[16] H. Tang, Y. Su, B. Chi, J. Zhao, D. Dang, X. Tian, S. Liao, G.-R. Li, Nodal PtNi nanowires with Pt skin and controllable Near-Surface composition for enhanced oxygen reduction electrocatalysis in fuel cells, Chem. Eng. J. 418 (2021), 129322.

[17] Q. Li, L. Li, X. Yu, X. Wu, Z. Xie, X. Wang, Z. Lu, X. Zhang, Y. Huang, X. Yang, Ultrafine platinum particles anchored on porous boron nitride enabling excellent stability and activity for oxygen reduction reaction, Chem. Eng. J. 399 (2020), 125827.

[18] H. Wan, F. Chen, W. Ma, X. Liu, R. Ma, Advanced electrocatalysts based on two-dimensional transition metal hydroxides and their composites for alkaline oxygen reduction reaction, Nanoscale 12 (42) (2020) 21479–21496.

[19] H.A. Firouzjaie, W.E. Mustain, Catalytic advantages challenges, and priorities in alkaline membrane fuel cells, ACS Catal. 10 (1) (2020) 225–234.

[20] P. Tan, Z. Wu, B. Chen, H. Xu, W. Cai, M. Ni, Exploring oxygen electrocatalytic activity and pseudocapacitive behavior of Co_3O_4 nanoplates in alkaline solutions, Electrochim. Acta 310 (2019) 86–95.

[21] J.A. Zamora Zeledon, M.B. Stevens, G. Gunasooriya, A. Gallo, A.T. Landers, M. E. Kreider, C. Hahn, J.K. Norskov, T.F. Jaramillo, Tuning the electronic structure of Ag-Pd alloys to enhance performance for alkaline oxygen reduction, Nat Commun 12 (1) (2021) 620.

[22] G. Meng, Z. Chang, X. Cui, H. Tian, Z. Ma, L. Peng, Y. Chen, C. Chen, J. Shi, SnO_2/CeO_2 nanoparticle-decorated mesoporous ZSM-5 as bifunctional electrocatalyst for HOR and ORR, Chem. Eng. J. 417 (2021) 127913.

[23] A. Holewinski, J.-C. Idrobo, S. Linic, High-performance Ag-Co alloy catalysts for electrochemical oxygen reduction, Nat Chem 6 (9) (2014) 828–834.

[24] L. Yuan, L. Jiang, J. Liu, Z. Xia, S. Wang, G. Sun, Facile synthesis of silver nanoparticles supported on three dimensional graphene oxide/carbon black composite and its application for oxygen reduction reaction, Electrochim. Acta 135 (2014) 168–174.

[25] L. Zeng, T.S. Zhao, L. An, A high-performance supportless silver nanowire catalyst for anion exchange membrane fuel cells, J. Mater. Chem. A 3 (4) (2015) 1410–1416.

[26] A. Qaseem, F. Chen, X. Wu, R.L. Johnston, Pt-free silver nanoalloy electrocatalysts for oxygen reduction reaction in alkaline media, Catal. Sci. Technol. 6 (10) (2016) 3317–3340.

[27] J.K. Nørskov, J. Rossmeisl, A. Logadottir, L. Lindqvist, J.R. Kitchin, T. Bligaard, H. Jónsson, Origin of the overpotential for oxygen reduction at a fuel-cell cathode, J. Phys. Chem. B 108 (46) (2004) 17886–17892.

[28] F.H.B. Lima, J.F.R. de Castro, E.A. Ticianelli, Silver-cobalt bimetallic particles for oxygen reduction in alkaline media, J. Power Sources 161 (2) (2006) 806–812.

[29] D.A. Slanac, W.G. Hardin, K.P. Johnston, K.J. Stevenson, Atomic ensemble and electronic effects in Ag-rich AgPd nanoalloy catalysts for oxygen reduction in alkaline media, J Am Chem Soc 134 (23) (2012) 9812–9819.

[30] K. Shin, D.H. Kim, H.M. Lee, Catalytic characteristics of AgCu bimetallic nanoparticles in the oxygen reduction reaction, ChemSusChem 6 (6) (2013) 1044–1049.

[31] Y. Wang, X. Lu, Y. Liu, Y. Deng, Silver supported on Co_3O_4 modified carbon as electrocatalyst for oxygen reduction reaction in alkaline media, Electrochem. Commun. 31 (2013) 108–111.

[32] Y. Yang, H. Fei, G. Ruan, L. Li, G. Wang, N.D. Kim, J.M. Tour, Carbon-free electrocatalyst for oxygen reduction and oxygen evolution reactions, ACS Appl Mater Interfaces 7 (37) (2015) 20607–20611.

[33] A. Yu, C. Lee, N.-S. Lee, M.H. Kim, Y. Lee, Highly efficient silver-cobalt composite nanotube electrocatalysts for favorable oxygen reduction reaction, ACS Appl Mater Interfaces 8 (48) (2016) 32833–32841.

[34] Q. Wang, F. Chen, Y. Liu, N. Zhang, L. An, R.L. Johnston, Bifunctional electrocatalysts for oxygen reduction and borohydride oxidation reactions using Ag_3Sn nanointermetallic for the ensemble effect, ACS Appl Mater Interfaces 9 (41) (2017) 35701–35711.

[35] Q. Wang, F. Chen, Y. Liu, T.T. Gebremariam, J. Wang, L. An, R.L. Johnston, AgSn intermetallics as highly selective and active oxygen reduction electrocatalysts in membraneless alkaline fuel cells, J. Power Sources 404 (2018) 106–117.

[36] Daily Metal Prices. https://www.dailymetalprice.com/.

[37] Z.H. Yonggang Yao, Pengfei Xie, Steven D. Lacey, Rohit Jiji Jacob, Hua Xie, Fengjuan Chen, Anmin Nie, Tiancheng Pu, Miles Rehwoldt, Daiwei Yu, Michael R. Zachariah, Chao Wang, Reza Shahbazian-Yassar, Ju Li, Liangbing Hu, Carbothermal shock synthesis of high-entropy-alloy nanoparticles, Science 359 (2018) 1489–1494.

[38] B.H.K. Chunpeng Yang, Sooyeon Hwang, Zhenyu Liu, Yonggang Yao, Wesley Luc, Mingjin Cui, Arnav S. Malkani, Tangyuan Li, Xizheng Wang, Jiaqi Dai, Bingjun Xu, Guofeng Wang, Dong Su, Feng Jiao, Liangbing Hu, Overcoming immiscibility toward bimetallic catalyst library, Sci. Adv. 6(17) (2020) 6844.

[39] Y. Yao, Z. Huang, P. Xie, L. Wu, L. Ma, T. Li, Z. Pang, M. Jiao, Z. Liang, J. Gao, Y. He, D.J. Kline, M.R. Zachariah, C. Wang, J. Lu, T. Wu, T. Li, C. Wang, R. Shahbazian-Yassar, L. Hu, High temperature shockwave stabilized single atoms, Nat Nanotechnol 14(9) (2019) 851-857.

[40] Y. Chen, G.C. Egan, J. Wan, S. Zhu, R.J. Jacob, W. Zhou, J. Dai, Y. Wang, V. A. Danner, Y. Yao, K. Fu, Y. Wang, W. Bao, T. Li, M.R. Zachariah, L. Hu, Ultra-fast self-assembly and stabilization of reactive nanoparticles in reduced graphene oxide films, Nat Commun 7 (2016) 12332.

[41] F. Chen, Y. Yao, A. Nie, S. Xu, J. Dai, E. Hitz, Y. Li, A. Lu, Z. Huang, T. Li, R. Shahbazian-Yassar, L. Hu, High-Temperature Atomic Mixing toward Well-Dispersed Bimetallic Electrocatalysts, Adv. Eng. Mater. 8(25) (2018) 1800466.

[42] Z. Ma, H. Tian, G. Meng, L. Peng, Y. Chen, C. Chen, Z. Chang, X. Cui, L. Wang, W. Jiang, J. Shi, Size effects of platinum particles@CNT on HER and ORR performance, Sci. China Mater. 63(12) (2020) 2517-2529.

[43] B. Xu, H. Yang, G. Zhou, X. Wang, Strong metal-support interaction in size-controlled monodisperse palladium-hematite nano-heterostructures during a liquid-solid heterogeneous catalysis, Sci. China Mater. 57 (1) (2014) 34–41.

[44] R. Majee, A. Kumar, T. Das, S. Chakraborty, S. Bhattacharyya, Tweaking nickel with minimal silver in a heterogeneous alloy of decahedral geometry to deliver platinum-like hydrogen evolution activity, Angew Chem Int Ed Engl 59 (7) (2020) 2881–2889.

[45] X. Ge, A. Sumboja, D. Wuu, T. An, B. Li, F.W.T. Goh, T.S.A. Hor, Y. Zong, Z. Liu, Oxygen reduction in alkaline media: from mechanisms to recent advances of catalysts, ACS Catal. 5 (8) (2015) 4643–4667.

[46] R.E. Davis, G.L. Horvath, C.W. Tobias, The solubility and diffusion coefficient of oxygen in potassium hydroxide solutions, Electrochim. Acta 12 (3) (1967) 287–297.

[47] G. Kresse, J. Furthmüller, Efficiency of ab-initio total energy calculations for metals and semiconductors using a plane-wave basis set, Comput. Mater. Sci. 6 (1) (1996) 15–50.

[48] N.X.V. Wang, J.-C. Liu, G. Tang, W.T. Geng, VASPKIT: a pre- and post-processing program for VASP code, Comput. Phys. Commun. 267 (2021), 108033.

[49] L. Yu, X. Pan, X. Cao, P. Hu, X. Bao, Oxygen reduction reaction mechanism on nitrogen-doped graphene: a density functional theory study, J. Catal. 282 (1) (2011) 183–190.

[50] H. Okamoto, Supplemental Literature Review of Binary Phase Diagrams: Ag-Co, Ag-Er, Ag-Pd, B-Ce, Bi-La, Bi-Mn, Cu-Ge, Cu-Tm, Er-Y, Gd-Tl, H-La, and Hg-Te, J. Phase Equilib. Diffus. 36 (1) (2014) 10–21.

[51] Q. Zhang, S. Tao, J. Du, A. He, Y. Yang, C. Tao, A cold plasma-activated in situ AgCo surface alloy for enhancing the electroreduction of CO_2 to ethanol, J. Mater. Chem. A 8 (17) (2020) 8410–8420.

[52] Y. Chen, J. Li, G. Yue, X. Luo, Novel Ag@nitrogen-doped porous carbon composite with high electrochemical performance as anode materials for lithium-ion batteries, Nanomicro Lett 9 (3) (2017) 32.

[53] Y. Garsany, O.A. Baturina, K.E. Swider-Lyons, S.S. Kocha, Experimental methods for quantifying the activity of platinum electrocatalysts for the oxygen reduction reaction, Anal. Chem. 82 (15) (2010) 6321–6328.

[54] H.M.A. Amin, C.J. Bondue, S. Eswara, U. Kaiser, H. Baltruschat, A Carbon-free Ag–Co_3O_4 composite as a bifunctional catalyst for oxygen reduction and evolution: spectroscopic, Microscopic and Electrochemical Characterization, Electrocatalysis 8 (6) (2017) 540–553.

[55] J.K. Nørskov, Fundamental concepts of heterogenous catalysis, John Wiley & Sons, Inc.2014.